Digitally Controlled Analog Cancellation for Full Duplex Broadband Power Line Communications

Gautham Prasad, Lutz Lampe, and Sudip Shekhar

***Abstract*—Although in-band full-duplexing (IBFD) has long been implemented in various communication media, it was only recently that an IBFD solution was presented for broadband power line communications (BB-PLC). The maximum attainable echo suppression using this solution is however limited by the dynamic range of the analog-to-digital converter (ADC). To counter this critical constraint, we propose echo cancellation in the analog domain, while persisting with a low-complexity frequency domain digital echo estimation. By formulating an expression for the number of ADC bits lost in IBFD over a conventional half-duplex operation, we show that the ADC dynamic range is no longer a limiting factor for our solution. We further extend our solution to present an analog cancellation method for multiple-input multiple-output IBFD BB-PLC systems. Finally, we present simulation results of echo cancellation and data rate gains obtained under realistic in-home BB-PLC settings, to demonstrate that our solution is capable of doubling bidirectional transfer rates in a large number of the tested network conditions.**

***Index Terms*—Full Duplex, Echo Cancellation, Broadband Power Line Communication (BB-PLC), Analog Cancellation, Quantization Noise, Multiple-Input Multiple-Output (MIMO) PLC**

I. Introduction

THE ability to transmit and receive data simultaneously in the same frequency band and over the same power line not only improves spectral efficiency, but also provides several significant networking benefits, like doubling the transmission efficiency in multi-hop relay networks, providing a resource-efficient solution to the classical hidden-node problem, and enabling spectrum-aware data transmission [1]–[4]. The primary impediment in achieving this in-band full-duplex (IBFD) operation is the interference of the transmitted signal with the received signal-of-interest (SOI). This interference, commonly referred to in literature as self-interference (SI) or echo, can be removed using one or more of the many echo cancellation (EC) techniques that have long been used in various communication systems [4]–[9].

EC methods can be broadly classified into two categories: suppression and cancellation [4]. Suppression involves attenuating the SI using techniques like antenna spacing [3], antenna separation [10], or antenna isolation [11], for multi-antenna transceivers. In case of single antenna transceivers, suppression is achieved through the use of a circulator or hybrid module that isolates the bidirectional signals [4], [12]. On the other hand, cancellation is performed by introducing a canceling signal either in the analog or digital domain to remove the echo component present in the received signal [4], [13]. One or more of these suppression and cancellation techniques are chosen in different IBFD communication systems depending on their requirements. For example, a full-duplex digital subscriber line (DSL) communication uses a hybrid and digital cancellation to achieve a target signal-to-interference-plus-noise ratio (SINR) performance [7], [14], whereas wireless IBFD communication typically uses one of the suppression techniques along with both analog and digital cancellation [4], [13].

The authors are with the Department of Electrical and Computer Engineering, The University of British Columbia, Vancouver, Canada. (e-mail: gauthamp@ece.ubc.ca; lampe@ece.ubc.ca; sudip@ece.ubc.ca).

A part of this work has been presented at the IEEE International Symposium on Power Line Communications and its Applications (ISPLC), Madrid, Spain, April 2017 [1].

This work was supported by the Natural Sciences and Engineering Research Council of Canada (NSERC).

A. State-of-the-art in IBFD for Broadband Power Line Communications

Although IBFD has historically been used in applications such as RADAR and telephone systems [5], [6], it was only recently that a feasible solution was proposed for broadband power line communications (BB-PLC) [2], [15]. Unlike full-duplex solutions for single-carrier narrowband PLC that use a hybrid module and a simple time-domain digital canceler [16], [17], our solution in [15] enables IBFD for the much larger bandwidth and sampling rate and the high channel attenuations experienced in BB-PLC scenarios.

The work in [2], [15] focused on the design of a custom hybrid and a mixed-domain digital EC procedure, and accomplished up to 63 dB of echo cancellation gain (ECG). While this was sufficient to significantly increase data rates in typical in-home BB-PLC scenarios, an ECG of up to 80 dB is typically required to bring the SI level down to the minimum power line noise floor [2], [15], [18], [19]. The solution of [15] chose not to use analog interference cancellation (AIC) techniques as they suffer from adaptivity and reconfigurability issues under rapidly changing echo channel conditions, which is commonly the case in PLC environments where any network change is reflected in the echo channel response. However, the maximum ECG achieved by this solution, which we will henceforth refer to as the digital interference cancellation (DIC) solution, is limited by the dynamic range of the analog-to-digital converter (ADC) used at the receiver. The quantization noise and distortion introduced by the ADC restricts the achievable ECG due to insufficient pre-digital isolation. This motivates us to investigate AIC methods, either to complement DIC or function independently, that are capable of not only countering the critical ADC dynamic range constraint but

also of providing precise adaptivity and reconfigurability. This would allow us to further improve the achievable ECG and accomplish a two-times data rate gain (DRG) in a broader range of in-home power line network conditions.

B. Contributions and Outline

In Section II, we first motivate the choice and applicability of our AIC design approach to BB-PLC systems, as opposed to other AIC techniques available in the literature. We present the details of our proposed solution in Section III, where we analyze its impact on the distortion and quantization noise produced by the ADC. Further, we relate this ADC distortion and quantization noise to the loss of precision in the ADC for quantizing the SOI, by formulating the number of ADC bits lost for resolving the residual SI. For this purpose, we also derive an approximate expression for the signal-to-noise-and-distortion ratio of the ADC that operates on an orthogonal frequency division multiplexed (OFDM) signal. We eventually show that by using our solution, we lose nearly zero ADC bits for resolving the residual SI. Next, in Section IV, we adapt our proposed solution to a generic multiple-input multiple-output (MIMO) BB-PLC scenario. We present our solution by describing its implementation at the PLC signal coupling interface and by analytically characterizing the interference channel transfer functions at the receivers of an IBFD-enabled MIMO BB-PLC device. Further, in Section V, we analyze the effects of non-linear SI components on EC, as they become more pronounced due to the reduction in ADC distortion and quantization noise. We then present simulation results of the performance of our proposed solution in Section VI for both single-input single-output (SISO) and MIMO configurations under realistic in-home PLC channel and noise environments, and compare it to the performance of the DIC solution under a similar setup. Finally, in Section VII, we provide a discussion on our proposed solution by describing the notable features and the costs associated with a practical implementation. We conclude the paper in Section VIII.

Nomenclature: $x(t)$ is used to represent a continuous time analog signal x at any time instant t, and $x[n] = x(nT_s)$ is its discrete time counterpart sampled with a frequency of $1/T_s$. $X[k] = \mathscr{F}_N\{x[n]\}$ is used to denote the frequency domain version of $x[n]$, where $\mathscr{F}_N\{\cdot\}$ is the discrete Fourier transform (DFT) operator of size N. $\boldsymbol{X} = [X[k]]^{\mathrm{T}}$ is the vector of all $X[k], \forall k \in \mathscr{N}$, where $\mathscr{N}$ $(|\mathscr{N}| \leq N)$ is the set of all data carrying sub-carriers. BB-PLC regulations across geographical locations restrict the usage of certain intermediate frequencies in the $2-100$ MHz bandwidth to protect non-PLC service frequencies such as amateur radio's HAM bands, citizen band, aeronautical bands, etc. [20]. $\mathscr{N}$ contains the non-contiguous set of sub-carriers that are not excluded by such regulations, and are used by BB-PLC devices for data transfer.

II. Analog SI Cancellation Solutions

AIC ensures that the residual SI does not introduce ADC distortion and quantization noise that is large enough to limit the achievable ECG. Several AIC techniques are available in the literature, which are used in full-duplex systems across communication media, e.g., [8], [9], [12], [13], [21]. A least mean square (LMS) adaptive analog cancellation solution was proposed in [8] for full-duplex Ethernet communication, where a four-tap analog finite impulse response (FIR) filter was used to estimate and cancel the echo in time domain. However, it has been shown in [15] that a time domain canceler for BB-PLC requires at least 40 taps to completely capture the effects of the echo channel. Extending the structure in [8] to 40 taps requires using 40 additional digital-to-analog converter (DAC) units, which is both costly and introduces additional distortions. Further, this solution and similar ones only managed to achieve ECG of about 20 dB, which is sufficient in Ethernet systems to prevent ADC saturation and allow subsequent digital cancellations of the echo and near-end crosstalk [22], [23]. However, these values are highly insufficient for BB-PLC scenarios that require ECG of up to 80 dB. A similar AIC technique with sign-sign LMS adaptation filters was also proposed for coaxial cable communications in [9], providing a gain of only about 15 dB.

Improved ECGs were obtained by a delay-line based AIC solution proposed for wireless IBFD systems [12], where a part of the transmitted analog signal was passed through delay lines of different lengths to recreate the attenuation and propagation delay experienced by the echo in the SI channel. However, such a solution is not applicable for BB-PLC scenarios where the echo consists of multiple notable signal reflections that are caused from discontinuities along the power lines. Recreating such long delays would require excessively lengthy delay lines. Alternatively, an adaptive AIC method for wireless systems was introduced in [13], similar to the ones in [8], [9]. Although this solution manages to achieve sufficient ECG, multi-tap FIR filter realization in the analog domain restricts the ability to quickly reconfigure filter weights and delays to widely varying PLC channel conditions. Thus, an analog cancellation solution that incorporates digital echo estimation is appropriate for IBFD PLC scenarios.

IBFD designs with analog cancellation and digital estimation were implemented for wireless communication systems in [10], [21], [24]. However, these solutions are not adaptive in nature. The echo estimator relies on a rather long silent period per frame, where the transceiver operates in half-duplex mode, to provide a least squares channel estimate. A slowly varying wireless echo channel between the transmitter and receiver antenna facilitates such an operation. In case of BB-PLC scenarios, the variation in the echo channel is driven by the changes in the overall PLC network. Hence, an adaptive channel estimation is more suitable. Next, since RF systems use mixers in the transmit and receive chains, digitally controlled AIC does not counter the additional phase noise and I/Q imbalance that limit the performance of such IBFD systems [4]. Hence, for wireless systems, AIC solutions that tap-in and process the transmitted signal in the analog domain provide greater SI cancellation, as they are able to better capture the above stated effects [4], [12]. Since typical BB-PLC systems operate completely in baseband, we do not face this limitation. This allows us to implement a digitally controlled AIC to obtain sufficient ECGs, uninhibited by phase noise or I/Q imbalance constraints. Since the digital echo

estimation of [10], [21], [24] does not completely capture the effects of analog RF components, they rely primarily on suppression techniques, like antenna separation, to provide the required SI attenuation. On the other hand, we use a single "antenna" transceiver system where we use the same power line conductor-pair for bidirectional communication. Alternatively, the coupling loss between multiple conductor-pairs could be exploited to achieve "antenna separation". Although this coupling loss between the conductor-pairs provides an isolation of about 12 dB, which is higher than that achieved with the hybrid module used in a "single-antenna" system [25], we show through our results that our solution achieves the target ECG using the single wire-pair configuration. Additionally, a higher suppression adversely affects the cancellation performance as our LMS adaptation algorithm relies on the relative strength of the echo component in the received signal. Furthermore, this multi-conductor setup does not provide us the physical flexibility of freely placing "antennas", and would only double the resources (conductor-pairs) used for transmission. Thus, we propose an IBFD solution that achieves simultaneous in-band bidirectional communication on the same wire-pair by relying predominantly on cancellation for EC. Finally, we address the distinctive challenges posed by the PLC coupling mechanism for an IBFD implementation, which have not been studied in any of the above.

In the following sections, we present our proposed adaptive AIC solution, where we cancel the echo in the analog domain by digitally estimating the echo channel. We use a one-tap FIR filter per sub-carrier to estimate the channel frequency response with minimal complexity using an adaptive LMS update algorithm. We then demonstrate the procedure to extend our solution to a MIMO BB-PLC scenario.

III. Proposed AIC Solution

A. System Model

We consider a point-to-point full-duplex BB-PLC link with two identical transceivers at each end, where the transmitter transmits an OFDM signal, x. The signal is coupled on to the power line with an active hybrid circuit used in between the analog front-end (AFE) and the PLC coupler [15]. The hybrid isolates x and the continuous time received signal, y, which is expressed as

$$y(t) = \underbrace{(x * h_{\mathrm{SI}})(t)}_{\text{echo}} + \underbrace{(x_{\mathrm{SOI}} * h_{\mathrm{PLC}})(t)}_{\text{signal-of-interest}} + \underbrace{r(t)}_{\text{cumulative noise}}, \quad (1)$$

where '$*$' indicates linear convolution, h_{SI} is the impulse response of the SI channel, x_{SOI} is the signal transmitted by the far-end transmitter traveling through a PLC channel with impulse response h_{PLC}, and r is the cumulative noise seen at the near-end receiver. The received signal is then passed through a receiver-end attenuator (RXA) that is present to handle large signals possibly transmitted from a nearby outlet. To accomplish cancellation at the receiver, an adaptive echo canceler uses a copy of x to generate an echo estimate, $\hat{y}$, which is subtracted from the received signal, y. The resultant error signal, $y-\hat{y}$, is fed back to the estimator to adapt its filter weights to produce an improved estimate in the next iteration.

B. Proposed Echo Cancellation Procedure

A block diagram of an IBFD-enabled transceiver with our proposed solution is shown in Fig. 1. We perform signal cancellation in the analog domain using an active differential amplifier circuit to obtain an error signal, e, given by

$$e(t) = y(t) - \hat{y}(t). \quad (2)$$

We then convert $e(t)$ to discrete time samples using an ADC, which is preceded by a programmable gain amplifier (PGA). A gain control module forces the PGA to scale the input signal appropriately to minimize the distortion and quantization noise introduced by the ADC. We use this scaling factor to de-scale the quantized error, $e[n]$, and send these digital samples to an FIR filter that we implement alike the one employed in the DIC solution [15]. We adapt the filter-weights vector, $\boldsymbol{W}(\ell)$, using the LMS adaptive update algorithm at every ℓth iteration, which corresponds to the ℓth OFDM block, as [26, Ch. 5]

$$\boldsymbol{W}(\ell+1) = \boldsymbol{W}(\ell) + \mu \mathrm{diag}(\boldsymbol{X}(\ell))^{*} \boldsymbol{E}(\ell)\ , \quad (3)$$

where $(\cdot)^{*}$ is the complex conjugation operator, μ is the step-size of the LMS update, and $\boldsymbol{X}(\ell)$ and $\boldsymbol{E}(\ell)$ are the frequency domain versions of $x[n]$ and $e[n]$, respectively[1]. Next, we obtain the echo estimate,

$$\hat{\boldsymbol{Y}}(\ell) = \boldsymbol{X}(\ell) \circ \boldsymbol{W}(\ell), \quad (4)$$

where '$\circ$' represents the Hadamard product. We then transform $\hat{\boldsymbol{Y}}(\ell)$ to time domain and convert it to a continuous analog signal, $\hat{y}$, using an additional DAC in the echo reconstruction chain. We also include a PGA after the DAC to provide any further amplification required.

Since we cancel the echo in the analog domain as per (2), the signal entering the PGA at the receiver has a lower power as the LMS adaptation improves the accuracy of $\hat{y}$. As a result of reduction in the total power of the signal entering the PGA, the distortion and quantization noise introduced by the ADC also decreases.

C. ADC Distortion and Quantization Noise

The power of the quantization and distortion noise introduced by the ADC is given by

$$P_{\mathrm{N,ADC}} = \frac{\sigma^2_{\mathrm{inp}}}{\gamma_{\mathrm{ADC}}}, \quad (5)$$

where σ^2_{inp} is the power of the input signal entering the quantizer, and γ_{ADC} is signal-to-noise-and-distortion ratio of the ADC. σ^2_{inp} is primarily driven by the transmit signal power and the extent of pre-digital EC. In case of the DIC solution of [15], pre-digital EC is achieved by hybrid suppression. Therefore, $\sigma^2_{\mathrm{inp}} = P_{\mathrm{TX}}G_{\mathrm{hyb}} + P_{\mathrm{TX}}G_{\mathrm{PLC}} + P_{\mathrm{N}}$, where P_{TX} is the transmit signal power used by both near- and far-end transmitters, G_{hyb} is suppression gain obtained by the hybrid, G_{PLC} is power line channel attenuation, and P_{N} is overall

[1]Please refer to Section I-B for the nomenclature used.

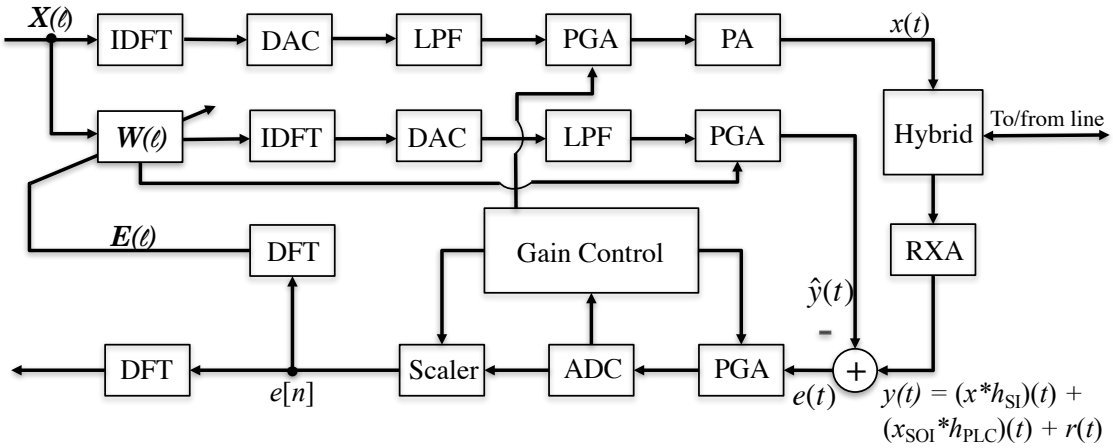

Fig. 1. Transceiver block diagram of an IBFD BB-PLC system with our proposed AIC solution. External band-pass filter and transient protection circuitry are not explicitly shown. DAC: Digital-to-analog converter, LPF: low-pass filter, PA: power amplifier.

noise power at the near-end receiver (not including ADC-induced noise)[2]. Hence, the power of the ADC distortion and quantization noise is

$$P_{\mathrm{N,ADC}}^{(\mathrm{DIC})} = \frac{P_{\mathrm{TX}}(G_{\mathrm{hyb}} + G_{\mathrm{PLC}}) + P_{\mathrm{N}}}{\gamma_{\mathrm{ADC}}}. \tag{6}$$

Due to the relatively low isolation typically provided by the hybrid (see [15, Fig. 2, 4(b)]), $G_{\mathrm{hyb}} \gg G_{\mathrm{PLC}}$, and $P_{\mathrm{N,ADC}}^{(\mathrm{DIC})} \approx {P_{\mathrm{TX}}G_{\mathrm{hyb}}}/{\gamma_{\mathrm{ADC}}}$.

However, pre-digital cancellation in our proposed solution contains both hybrid suppression and the AIC. Therefore, σ_{inp}^2 is a function of the LMS iteration, ℓ, and reduces with increasing ℓ. We have $\sigma_{\mathrm{inp}}^2(\ell) = P_{\mathrm{TX}}G_{\mathrm{hyb}}G_{\mathrm{AIC}}(\ell) + P_{\mathrm{TX}}G_{\mathrm{PLC}} + P_{\mathrm{N}}$, where $G_{\mathrm{AIC}}(\ell)$ is the AIC gain produced in the ℓth LMS iteration. Hence, the power of the ADC distortion and quantization noise is

$$P_{\mathrm{N,ADC}}^{(\mathrm{AIC})}(\ell) = \frac{P_{\mathrm{TX}}(G_{\mathrm{hyb}}G_{\mathrm{AIC}}(\ell) + G_{\mathrm{PLC}}) + P_{\mathrm{N}}}{\gamma_{\mathrm{ADC}}}. \tag{7}$$

As the accuracy of $\hat{y}$ increases with ℓ and G_{AIC} approaches zero, $P_{\mathrm{N,ADC}}^{(\mathrm{AIC})}(\ell)$ tends toward the value of $P_{\mathrm{N,ADC}}$ observed under a half-duplex (HD) operation. This assures that $P_{\mathrm{N,ADC}}^{(\mathrm{AIC})}$ is no longer a limiting factor for the achievable ECG.

D. Impact on ADC Bit Loss

To better understand the impact of distortion and quantization noise on the SOI and thus gain insight into the extent of degradation caused by IBFD operation, we map $P_{\mathrm{N,ADC}}$ to the number of ADC bits lost in an IBFD operation for quantizing the additional residual SI.

Due to the high peak-to-average-power ratio (PAPR) of OFDM signals, the gain control module lets the PGA scale the input signal to accommodate some clipping in the ADC, in order to minimize the overall clipping distortion and quantization noise [27]. Under such an operation, γ_{ADC} is given by [28]

$$\gamma_{\mathrm{ADC}}^{-1} = \frac{1/3}{2^{2m}}\left(\frac{V_{\mathrm{clip}}}{\sigma_{\mathrm{inp}}}\right)^2 + \sqrt{\frac{8}{\pi}}\left(\frac{\sigma_{\mathrm{inp}}}{V_{\mathrm{clip}}}\right)^3 \exp\left(\frac{-{V_{\mathrm{clip}}}^2}{2\sigma_{\mathrm{inp}}^2}\right), \tag{8}$$

where m is the ADC resolution, and any part of the input signal beyond a voltage $|V_{\mathrm{clip}}|$ is clipped. The number of ADC bits lost for quantizing the residual SI can be computed by determining the ADC dynamic range per-bit using (8). In Appendix A, we show that γ_{ADC} is approximately linear with m in logarithmic scale, and can be expressed as

$$\hat{\gamma}_{\mathrm{ADC,dB}} = 5.5m - 3.6, \tag{9}$$

where $\hat{\gamma}_{\mathrm{ADC,dB}}$ is a linear approximation of γ_{ADC} in dB. Clearly, the dynamic range of every bit of the ADC under our operation is 5.5 dB. Thus, we can represent the number of bits lost for quantizing the SOI as

$$b_{\mathrm{lost}} = \frac{10 \cdot \log_{10}\left(\frac{\sigma_{\mathrm{inp}}^2}{P_{\mathrm{TX}}G_{\mathrm{PLC}}}\right)}{5.5}. \tag{10}$$

In Appendix B, we show using (10) that the number of ADC bits lost for the quantization of the SOI in an IBFD operation is given by

$$b_{\mathrm{lost}} = \lambda \cdot \log_{10}\left(1 + \frac{P_{\mathrm{TX}}G_{\mathrm{total}}}{P_{\mathrm{TX}}G_{\mathrm{PLC}} + P_{\mathrm{N}}}\right), \tag{11}$$

where G_{total} is the total ECG of both suppression and cancellation before the ADC, and λ is a constant of value ${20}/{11}$.

As explained in Section III-C, pre-digital isolation in the DIC solution is achieved only using the hybrid. Therefore, $G_{\mathrm{total,DIC}} = G_{\mathrm{hyb}}$, while $G_{\mathrm{total,AIC}}$ includes the adaptive AIC, and is therefore a function of the LMS iteration, ℓ. Thus, $G_{\mathrm{total,AIC}}(\ell) = G_{\mathrm{hyb}}G_{\mathrm{AIC}}(\ell)$. This gives us

$$b_{\mathrm{lost,DIC}} = \lambda \cdot \log_{10}\left(1 + \frac{P_{\mathrm{TX}}G_{\mathrm{hyb}}}{P_{\mathrm{TX}}G_{\mathrm{PLC}} + P_{\mathrm{N}}}\right) \tag{12}$$

$$b_{\mathrm{lost,AIC}}(\ell) = \lambda \cdot \log_{10}\left(1 + \frac{P_{\mathrm{TX}}G_{\mathrm{hyb}}G_{\mathrm{AIC}}(\ell)}{P_{\mathrm{TX}}G_{\mathrm{PLC}} + P_{\mathrm{N}}}\right). \tag{13}$$

As $G_{\mathrm{AIC}}(\ell)$ reduces and approaches zero with increase in ℓ, (13) reduces to $b_{\mathrm{lost,AIC}}(\ell) \approx \lambda \log_{10}(1) = 0$.

[2]We do not explicitly indicate the attenuation of the RXA since it works along with the PGA of the ADC, and applies equally to both DIC and AIC scenarios.

IV. AIC FOR MIMO IBFD BB-PLC

In this section, we use our AIC design developed in Section III to propose an IBFD MIMO BB-PLC system. A MIMO operation is supported over power lines by utilizing the three conductors available in most in-home single-phase electrical installations [29]. For multi-phase electrical distribution infrastructures, more than three wires are available to support even more transmission streams [30, Ch. 13]. The usage of MIMO has also been ratified in the latest BB-PLC standards of HomePlug AV2 and ITU-T G.9963 [31], [32].

To propose an AIC solution for a MIMO system, we consider a point-to-point MIMO BB-PLC link with two IBFD-enabled nodes at each ends. The near-end node uses $N_{\mathrm{T}}^{\mathrm{near}}$ and $N_{\mathrm{R}}^{\mathrm{near}}$ active transmitters and receivers, respectively, while the far-end node uses $N_{\mathrm{T}}^{\mathrm{far}}$ and $N_{\mathrm{R}}^{\mathrm{far}}$. In typical in-home BB-PLC scenarios $N_{\mathrm{R}} > N_{\mathrm{T}}$, as the number of usable transmitter chains is limited by Kirchoff's law [29, Ch. 1]. However, the presence of parasitic components allows non-redundant information to be extracted from signals on all available conductor pairs. Furthermore, irrespective of the type of decoupling used for obtaining the differential signals, an additional reception mode can be realized through common-mode decoupling by extracting the common-mode signal on all the conductors [33]. This type of a structure can incorporate the hybrid circuit for suppression only on the N_{T} transceiver chains, as the hybrid isolates bidirectional signals on the same conductor pair. For the remaining $(N_{\mathrm{R}} - N_{\mathrm{T}})$ receiver chains, suppression can be accomplished through the coupling losses present across different conductor pairs. A conceptual structure of such a setup is shown in Fig. 2 for a single-phase power line infrastructure. The three available conductors, live/line/phase/hot (L), neutral (N), and ground/protective earth (PE), allow coupling and decoupling on a maximum of two transmitter chains ($N_{\mathrm{T}} = 2$) and four receiver chains ($N_{\mathrm{R}} = 4$), respectively.

Consider a near-end MIMO node with $N_{\mathrm{T}}^{\mathrm{near}}$ transmitter chains. This node transmits N_T^{near} OFDM signals, x_i, $i = 1, 2, ..., N_T^{\mathrm{near}}$, and receives $N_{\mathrm{T}}^{\mathrm{far}}$ streams. The ith received signal can be represented as

$$y_i(t) = \sum_{j=1}^{N_{\mathrm{T}}^{\mathrm{near}}} (x_j * h_{ij})(t) + \sum_{j=1}^{N_{\mathrm{T}}^{\mathrm{far}}} (x_{\mathrm{SOI},j} * h_{\mathrm{PLC},ij})(t) + r_i(t), \quad \forall i = 1, 2, ...N_{\mathrm{R}}^{\mathrm{near}} \tag{14}$$

where h_{ij} is the interference channel impulse response from the jth transmitter to the ith receiver at the near-end node, $x_{\mathrm{SOI},j}$ is the jth far-end transmitted signal, $h_{\mathrm{PLC},ij}$ is the power line channel impulse response from the jth far-end transmitter to the ith near-end receiver, and r_i is the cumulative pre-ADC noise at the ith receiver of the near-end node.

An echo estimate, $\hat{y}_i$, is generated by a filter bank present at every receiver chain. The echo estimate is removed from y_i, and the resultant error is sent back to the echo channel estimator for filter-weights adaptation.

A block diagram of the ith transceiver with our proposed AIC solution is shown in Fig. 3. Every transceiver associated with a hybrid also contains an identical structure, but with a different set of LMS filters. The LMS adaptive cancellation procedure is essentially an $N_{\mathrm{T}}^{\mathrm{near}}$-times scaled version of the SISO solution in Fig. 1. The $N_{\mathrm{T}}^{\mathrm{near}}$ filters estimate the SI and cross-interference (CI) channel transfer functions adaptively. The structure of the stand-alone receivers (i.e., receivers without an associated transmitter) is also similar to Fig. 3. While its structure does not contain a transmit chain and therefore no hybrid, it uses the same digital interference channel estimation and AIC procedure as in Fig. 3. Suppression in this case is achieved through coupling losses between the conductor pairs. In reference [15], we have already provided the suppression gain by deriving the echo channel transfer function at the transceivers through the hybrid, i.e., considering a 2×2 MIMO system with no stand-alone receivers. In Appendix C, we proceed further to derive the transfer function of the echo channel caused by the coupling losses between conductor-pairs at a stand-alone receiver using circuit theory approach. We show by way of numerical results in Section VI that the suppression obtained at the stand-alone receivers through coupling losses is nearly identical to that gained using the hybrid.

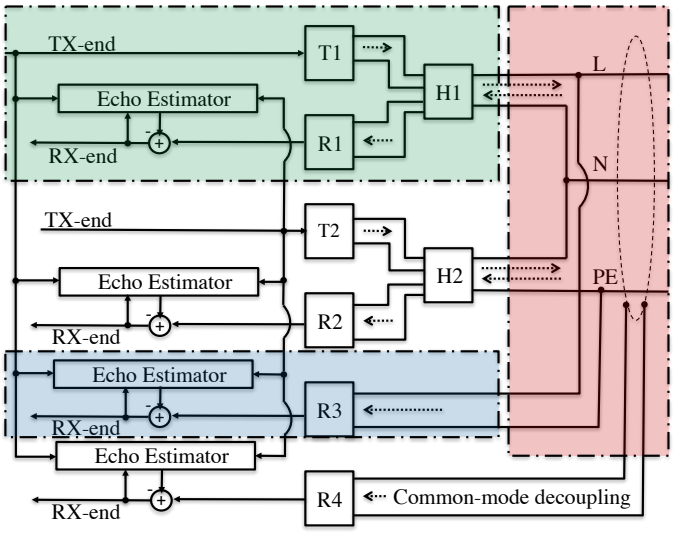

Fig. 2. A schematic representation of an IBFD-enabled 2×4 MIMO BB-PLC transceiver setup. The line-hybrid interface is highlighted in red, and the echo canceler of transceiver-1 and transceiver-3 are highlighted in green and blue, respectively. T and R indicate the front-ends of the transmitter and receiver chains, respectively, and H represents the hybrid.

The proposed MIMO-IBFD solution with analog EC provides similar reduction in ADC distortion and quantization noise to a SISO case, and consequently loses similar number of ADC bits in resolving the SI. The exact expression for the number of bits lost at every ith ADC is given by (26) in Appendix B.

V. EFFECT OF NON-LINEAR SI COMPONENTS

One of the implications of the significant reduction in $P_{\mathrm{N,ADC}}$ is that the non-linear components of the SI are no longer insignificant for EC, as it was the case in the DIC solution [15]. Non-linear components are typically generated by the active components in the transceiver. For baseband

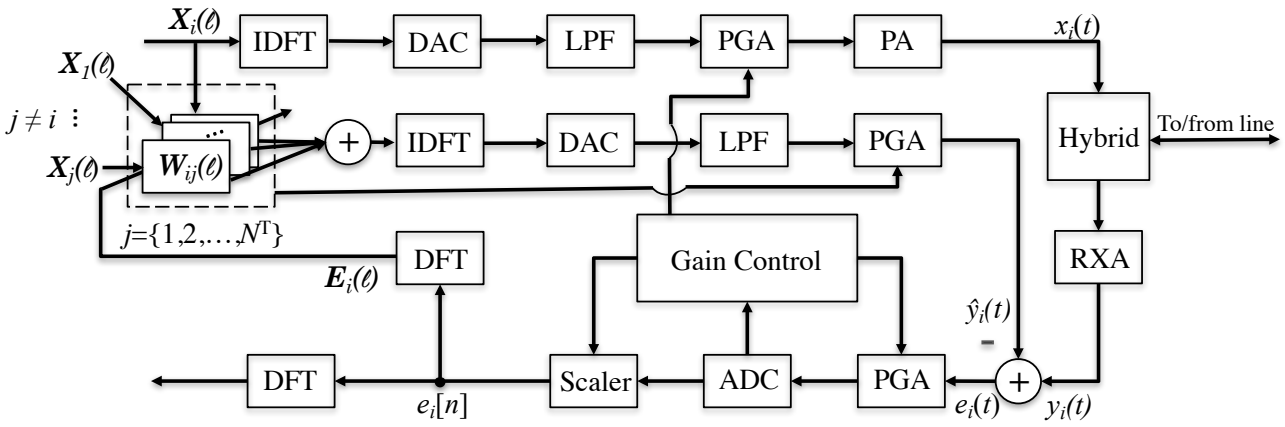

Fig. 3. A block diagram of the ith transceiver (shown in green in Fig. 2) of an $N_{\mathrm{T}} \times N_{\mathrm{R}}$ MIMO IBFD BB-PLC node with our proposed AIC. A similar structure follows for all N_{T} transceivers.

applications, non-linear SI components are largely generated by the amplifiers in the device. The total power of these components depends on the transmitted signal power and the type of amplifiers used. In the transmitter chain, the power amplifier (PA) is the main source of non-linear distortions as it operates with the largest signal power. Baseband PAs can be modeled using several different approaches [34]. Among these, the Hammerstein model is a generic baseband PA model using which the output signal of the PA can be written as [35]

$$x(t) = \sum_{\substack{p=1 \\ p \text{ odd}}}^{P} a_p \cdot x_\phi(t) \left(|x_\phi(t)|\right)^{p-1}, \tag{15}$$

where x_ϕ is the pre-amplified signal entering the PA, a_p is the scaling factor for the pth order of distortion, and P indicates the total number of significant orders of distortion. The summation is only over odd powers of p, since the components of $x_\phi(t)$ raised to even powers typically lie outside the band of interest for baseband signals. The term corresponding to $p = 1$ is the linear component of $x_\phi(t)$, while the others are the non-linear distortions introduced by the PA. We determine the scaling factors a_p, $\forall p > 1$, based on the specifications of the PA used by the transmitter. Typical PLC line drivers, such as [36], specify that the total non-linear distortions lie in the range of 75 dB to 80 dB below the transmit power. This amplified signal then passes through the hybrid, which we implement using active operational amplifiers (op-amps). Commercially available low-distortion op-amps can be used in this circuit to ensure insignificant non-linear distortions [37]. The echo then interferes with the SOI and enters the receiver chain. Unlike radio-frequency systems, BB-PLC receiver does not use a low-noise amplifier since the power line induced noise is significantly higher than the thermal noise floor. Instead, BB-PLC receivers use an RXA to handle a large signal that could possibly enter from a nearby power outlet. Baseband RXA can be implemented using simple passive components and thus does not contribute to any non-linear distortions.

The above analysis suggests that the total non-linear SI components are at least 75 dB below the transmit PSD. Thus, for a North American transmit PSD mask of -50 dBm/Hz [38, Ch. 4], non-linear components require a worst-case cancellation of up to 5 dB to bring them down to the minimum noise floor of -130 dBm/Hz that is typically seen in in-home BB-PLC networks for the considered transmission band [18], [19]. For the European transmit PSD limit of -55 dBm/Hz [39], the non-linear distortions are brought down to this noise floor without any additional cancellations required. Nevertheless, non-linear SI components undergo suppression through the hybrid. Although we obtain sufficient hybrid isolation of about 7 dB on an average, the isolation gain is frequency selective in nature. In particular, the gain obtained at a frequency f is given by [15]

$$G_{\mathrm{hyb}}(f) = c \cdot \left| \frac{Z_{\mathrm{PLC}}(f) - Z_{\mathrm{hyb}}(f)}{Z_{\mathrm{PLC}}(f) + Z_{\mathrm{hyb}}(f)} \right|^2, \tag{16}$$

where Z_{PLC} is the line impedance seen by the hybrid port connected to the power line, Z_{hyb} is the port impedance of the hybrid port connected to the line, and c is a scaling factor capturing the effects of impedance bridging and matching at the hybrid ports. Due to this frequency dependence, it has been shown in [15, Fig. 2] that the hybrid isolation can be as low as 2 dB for certain frequencies. In such a case, the worst-case PSD of the non-linear components, with a maximum transmit PSD of -50 dBm/Hz, lies 3 dB above the noise floor.

Toward proposing a low-complexity and a low-power overhead solution, we decide to tolerate the outlier scenario, without including a non-linear SI cancellation module either digitally, or by introducing an additional power-hungry PA in the echo reconstruction chain for analog non-linear cancellation.

VI. Simulation Results

In this section, we present numerical results of echo cancellation and practical data rate gains obtained by simulations performed under realistic BB-PLC channel and noise settings. We run our simulations with the proposed AIC scheme for both SISO and MIMO system configurations and compare our results with the performance of the DIC solution of [15].

A. Simulation Settings

Throughout our simulations, we use system parameters from the HomePlug AV standard [40]. We implement baseband OFDM using a fast Fourier transform of size 3072, with the North American amplitude map and tone mask specified in [40, Figure 3-24] and [40, Table 3-23], respectively. For SISO simulations, we implement the transceiver shown in Fig. 1 for our proposed AIC solution, and the transceiver block shown in [15, Fig. 3(b)] for a comparison with the DIC solution. For the MIMO configuration, we implement the transceivers for the AIC and DIC solutions as shown in Fig. 3 and [15, Fig. 13], respectively. To emulate the infinite precision analog signal, we use the default 64-bit double precision of MATLAB, and we use a 12-bit ADC with 11 effective number of bits to quantize the converted digital signal sampled at 75 MHz [40]. We model the power amplifier using (15), with a_1 set according to the amplitude map of the HomePlug AV standard, and a_p, $\forall p \neq 1$, set as per the non-linear distortion powers specified in [36].

B. Channel and Noise Models

We use the same channel and noise models employed in [15], since they provide comprehensive models for realistic in-home power line network settings, and also enable a fair comparison between our solutions. A detailed description of these is provided in [15, Appendix A]. For the sake of completeness, we mention the main features here.

1) Channel Generation: For the SISO case, we use the PLC channel generator tool of [41] that computes the channel transfer function using the bottom-up approach [42]. The tool provides a random network setting in which the number of derivation boxes and outlets, the positions of the transmitter and receiver, and the loads connected to each of the outlets are randomly varied to produce different channel frequency responses. We limit the number of derivation boxes and outlets to 15 to emulate a realistic indoor network. To obtain the transfer function of MIMO channels, we use the open-source MIMO PLC channel emulator tool of [43] that integrates power line parameter computation (e.g., [44]) and channel generation using multi-conductor transmission line theory (e.g., [45]). With a set tree topology in the simulator, we randomly vary the branch lengths, the loads connected to each outlet, and the type of power cable used. In order to replicate realistic in-home power line networks, we limit the number of outlet nodes and branches to 15 and 20, respectively, with a maximum branch length of 100 meters.

2) Noise Generation: To generate power line noise, we use our previously developed cumulative power line noise generator tool, where we model the power line noise as a sum of colored background noise, narrowband noise, periodic impulse noise synchronous with the alternating current (AC) mains cycle, periodic impulse noise asynchronous with the AC mains cycle, and aperiodic impulse noise [39, Annex. F]. We have made the tool available online [19] for the purposes of reproducibility and dissemination.

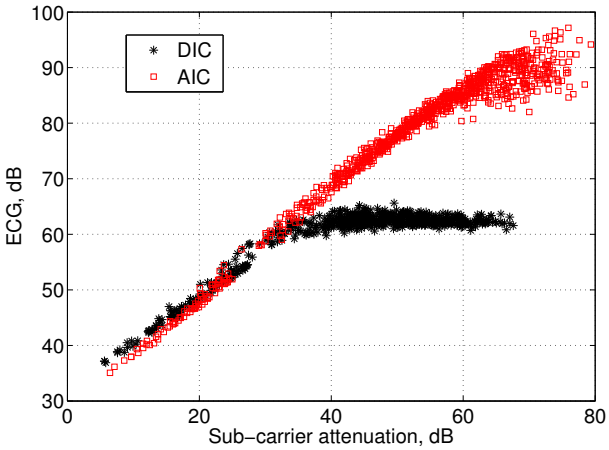

Fig. 4. Variation of ECG with sub-carrier PLC channel attenuation.

C. Numerical Results

1) Echo Cancellation Gain in SISO Mode: We define the ECG as the ratio of the SINR of the SOI after EC to SINR of the SOI before EC. To facilitate a precise data rate gain analysis in later sections, we compute the ECG on a per sub-carrier basis. Considering that one of either noise or the interference component dominates, we use the approximation,

$$\mathrm{ECG} \approx \frac{P_{\mathrm{TX}}}{\max\{P_{\mathrm{RSI}}, P_{\mathrm{N,ADC}}, P_{\mathrm{N}}\}}, \tag{17}$$

where P_{RSI} is the power of the residual SI including both linear and non-linear components. For the sake of brevity, we drop denoting the sub-carrier index in (17). ECG includes the effects of both suppression and cancellation. The cancellation gain is obtained from analog and digital LMS cancellation for the AIC and DIC solution, respectively, and is computed after the LMS iterations reach convergence.

Fig. 4 shows a scatter plot of the variation of ECG with the channel attenuation of the kth sub-carrier, $1/|H_{\mathrm{PLC}}[k]|^2$, over 1000 random channels generated using [41]. To isolate the interference cancellation ability of our proposed solution, we perform our simulations under zero-noise conditions. This ensures that the effects of RSI, and not the ambient noise, limit the achieved ECG. Since PLC noise is always an eventual limiting factor for the achieved ECG, overcoming the RSI limitation is the key performance indicator when comparing the DIC and our proposed AIC solutions. When P_{RSI} and $P_{\mathrm{N,ADC}}$ are sufficiently reduced, complete IBFD gains are achieved for any given P_{N} level.

We notice that, as with the DIC solution, the achieved ECG improves with increasing channel attenuation due to more accurate echo estimates [15]. Fig. 4 also demonstrates that while ECG for DIC is limited by $P_{\mathrm{N,ADC}}$, and hence saturates at around 63 dB, ECG for AIC continues to grow further with increase in channel attenuation to reach up to 90 dB. At this point ECG begins to saturate due to the presence of residual non-linear SI components. With our proposed AIC solution, we are able to obtain an ECG > 80 dB at higher sub-carrier attenuations, which is the target gain required to bring the

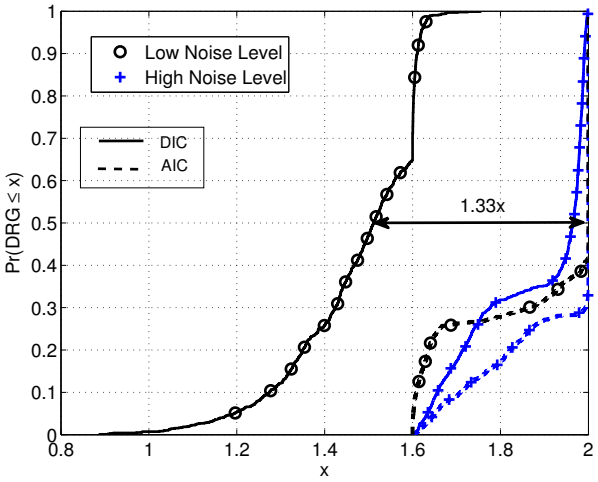

Fig. 5. CDF plots of DRGs obtained for a SISO IBFD system under two different noise levels using the DIC and AIC solutions, with DRG computed as (18).

SI down to the minimum noise floor commonly seen in in-home power line networks [15]. Reducing the SI level down to the noise floor allows true doubling of data rates. However, since we do not achieve $\mathrm{ECG} > 80$ dB under all sub-carrier attenuations, we do not successfully double data rates under all conditions.

2) Data Rate Gain in SISO Mode: The attainable DRG is not only dependent on ECG, but also on the prevalent noise conditions. Under a high noise scenario, a lower ECG is sufficient to double the data rate by bringing the SINR to the signal-to-noise ratio in the HD mode ($\mathrm{SNR}_{\mathrm{HD}}$), while a larger ECG is required under a low noise scenario. Hence, we expect to attain higher DRGs at higher noise levels, and lower gains at lower noise levels. In order to determine DRGs obtained under a low-noise scenario, we compute the theoretical gains with the DIC and AIC solutions for different sub-carrier attenuations in Table I. We use an adaptive bit loading algorithm [29, Ch. 9] that allocates bits on the kth sub-carrier with a quadrature amplitude modulation constellation size of M_k, based on the received sub-carrier SNR, $\mathrm{SNR}_{\mathrm{HD},k}$ or SINR_k, to maintain a target bit error rate (BER) P_b, expressed as [46, Eq. (8)]. We set $P_b = 10^{-3}$, which is a conservative target unencoded BER, and limit $M_k \leq 1024$ in accordance with the HomePlug AV specifications [38, Ch. 4]. We then compute $\mathrm{DRG}_{k,\phi} = \frac{2\log_2(M_{k,\phi})}{\log_2(M_{k,\mathrm{HD}})}$, for $\phi = \{\mathrm{AIC}, \mathrm{DIC}\}$. Since $P_{\mathrm{N,ADC}}$ limits the $\max(\mathrm{ECG})$ for the DIC solution, we observe in Table I that $\mathrm{DRG}_{k,\phi} < 1$ for higher sub-carrier attenuations (SCAs). In contrast, with our AIC solution, ECG continues to improve with increasing SCA and is able to achieve $\mathrm{DRG}_{k,\mathrm{AIC}} = 2$. However, we notice that under lower SCAs, we still encounter a sub-optimal $\mathrm{DRG}_{k,\mathrm{AIC}} < 2$ due to insufficient ECGs (see Fig. 4).

Since $\mathrm{DRG}_{k,\phi}$ is computed on a per sub-carrier basis, it is not indicative of the overall DRG that is eventually obtained. To investigate the overall DRGs that we can expect to procure under practical in-home PLC channel and noise scenarios, we simulate the transceiver block of Fig. 1 under two different noise levels. The cumulative PLC noise generator tool of [19] provides a control to generate noise samples at different levels by varying various noise parameters, for example, maximum amplitude of the impulses, or the roll-off factor of the colored background noise. We choose a low- and a high-noise setting in [19] to evaluate the achievable DRGs under the two extreme conditions. We compute the overall DRG in both these cases as the ratio of the physical layer sum-rate across all data carrying sub-carriers in IBFD and HD modes,

$$\mathrm{DRG}_{\phi} = \frac{2 \cdot \sum\limits_{k \in \mathcal{N}} \log_2(M_{k,\phi})}{\sum\limits_{k \in \mathcal{N}} \log_2(M_{k,\mathrm{HD}})}, \tag{18}$$

for $\phi = \{\mathrm{AIC}, \mathrm{DIC}\}$. Fig. 5 shows the cumulative distribution function (CDF) plot of DRGs obtained over 1500 random channel realizations that were generated using [41]. For typical power line noise conditions, we expect the CDF values of DRG to lie in between the two curves shown in Fig. 5 for both the DIC and AIC solutions. We observe that with the AIC solution, we are able to double the data rates for over 60% of the cases under high noise levels. Even under a low noise condition, we achieve $\mathrm{DRG}_{\mathrm{AIC}} \geq 1.6$, and eliminate any conditions under which $\mathrm{DRG} < 1$.

3) Echo Cancellation Gain in MIMO Mode: To determine the ECG in a MIMO IBFD system, we run simulations with an $N_{\mathrm{T}} \times N_{\mathrm{R}}$ MIMO configuration. Since most in-home installations are wired for single-phase power distribution, we use $N_{\mathrm{T}} = 2$. We also set $N_{\mathrm{R}} = 3$, where two of the receivers are associated with a transmitter each on the same conductor-pair with suppression achieved through a hybrid, and the other is a stand-alone receiver where the interference signal undergoes suppression as a result of the coupling losses between the conductor pairs. We use the interference channel transfer functions of the hybrid provided in [15] at the two transceivers. For suppression at the stand-alone receiver, we derive the channel transfer function in Appendix C as a function of the reflection co-efficient seen at the line-device interface.

Such a configuration produces SI and CI components that need to be canceled at each of the N_{R} receivers. We define ECG for both SI and CI individually as

$$\mathrm{ECG}_{\mathrm{SI}} = \frac{P_{\mathrm{TX}}}{\max\{P_{\mathrm{RSI}}, P_{\mathrm{N,ADC}}, P_{\mathrm{N}}\}} \tag{19}$$

$$\mathrm{ECG}_{\mathrm{CI}} = \frac{P_{\mathrm{TX}}}{\max\{P_{\mathrm{RCI}}, P_{\mathrm{N,ADC}}, P_{\mathrm{N}}\}}, \tag{20}$$

where P_{RCI} is the power of the residual CI including both linear and non-linear components. We refer to both interference signals at the stand-alone receiver as CIs, and compute $\mathrm{ECG}_{\mathrm{CI}}$ as (20).

Fig. 6 shows a smoothing spline fit of $\mathrm{ECG}_{\mathrm{SI}}$ and $\mathrm{ECG}_{\mathrm{CI}}$ for both DIC and AIC solutions, obtained at one of the two transceivers for 1000 random MIMO channels generated using [43]. The gains at the other transceiver are also identical. Similar to the results in Fig. 4, $\mathrm{ECG}_{\mathrm{SI}}$ and $\mathrm{ECG}_{\mathrm{CI}}$ for the AIC solution grow with increase in SCA without being limited by ADC distortion and quantization noise. We further observe that

TABLE I
A COMPARISON OF THE THEORETICAL DATA RATE GAINS PER SUB-CARRIER WITH DIC AND AIC SOLUTIONS UNDER DIFFERENT SUB-CARRIER ATTENUATIONS WITH A NOISE FLOOR OF −130 DBM/HZ.

SCA (dB)	$\mathrm{ECG}_{\mathrm{DIC},k}$ (dB)	$\mathrm{ECG}_{\mathrm{AIC},k}$ (dB)	$\mathrm{SNR}_{k,\mathrm{HD}}$ (dB)	$M_{k,\mathrm{HD}}$	$\mathrm{SINR}_{k,\mathrm{DIC}}$ (dB)	$M_{k,\mathrm{DIC}}$	$\mathrm{DRG}_{k,\mathrm{DIC}}$	$\mathrm{SINR}_{k,\mathrm{AIC}}$ (dB)	$M_{k,\mathrm{AIC}}$	$\mathrm{DRG}_{k,\mathrm{AIC}}$
5	37	36	75	1024	32	1024	**2**	31	1024	**2**
10	40	39	70	1024	30	256	**1.6**	29	256	**1.6**
20	47	47	60	1024	27	256	**1.6**	27	256	**1.6**
30	57	57	50	1024	27	256	**1.6**	27	256	**1.6**
40	61	68	40	1024	21	64	**1.2**	28	256	**1.6**
50	62	79	30	256	12	4	**<1**	30	256	**2**
60	62	85	20	16	2	2	**<1**	20	16	**2**
70	62	87	10	4	-8	1	**<1**	10	4	**2**

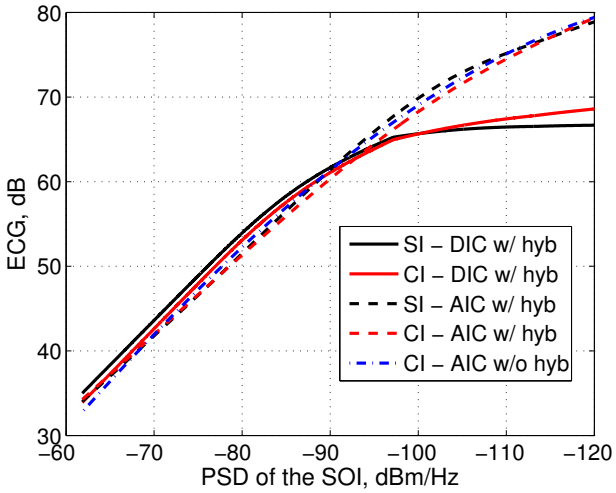

Fig. 6. Variation of ECG for SI (19) and CI (20) with sub-carrier attenuation, for the DIC and AIC solutions. A plot with hybrid represents the ECG at the receivers accompanied by a transmitter on the same conductor pair, while a plot without the hybrid indicates the ECG at the stand-alone receiver.

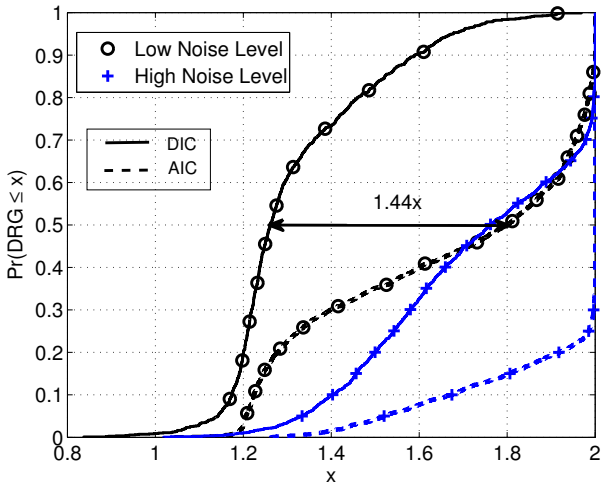

Fig. 7. CDF plots of DRGs obtained at one of the receivers of the MIMO IBFD system under two different noise levels using the DIC and AIC solutions, with DRG computed as (18).

the ECG for the CI at the stand-alone receiver (i.e., without the hybrid) also presents a similar curve, indicating analogous values of suppression. Note that we represent the x-axis as the PSD of the SOI to present results that are independent of the value of $N_{\mathrm{T}}^{\mathrm{far}}$.

4) Data Rate Gain in MIMO Mode: To determine the overall DRG that we can expect to gain under practical power line network conditions, we run the system shown in Fig. 3 under two different noise scenarios as used in Section VI-C2. The CDF plot of the DRGs computed as (18) is provided in Fig. 7, which is obtained for a set of 1500 random MIMO PLC channels [43]. Considering the results from Fig. 6, we show the DRG for the first receiver chain in Fig. 7. We observe that the AIC solution significantly improves DRGs compared to the use of the DIC solution, with $\mathrm{DRG}_{\mathrm{AIC}} = 2$ obtained for over 70% of the cases under a high noise level, and a median gain of 1.8 under low noise levels.

VII. DISCUSSION ON THE PROPOSED AIC SOLUTION

In this section, we reflect on our proposed AIC solution to discuss the salient features and provide costs associated with its implementation.

A. Notable Characteristics

1) Upward and Downward Compatibility: Although we use HomePlug AV specifications throughout our simulations, our echo estimation and cancellation procedure can be applied to any OFDM system with arbitrary number of sub-carriers and transmission/reception chains, i.e., our solution can be implemented on older HomePlug releases like HomePlug 1.0 as well as newer standards like HomePlug AV2, ITU-T G.9963, and other OFDM-based standards [31], [32].

2) Training Period: One of the marked features of our proposed solution is that it requires no additional start-up time or a silent training period that are typically required by most IBFD solutions commonly seen in other communication systems [3], [8], [10], [12]. The LMS filter that we use, adapts its filter weights using the received signal, by exploiting the higher power of the echo in the presence of the SOI. When a silent period is however available, where the transceiver is only transmitting, the filter weights adapt to their optimal value and provide the maximal ECG, i.e., the highest value in Figs. 4 and 6, for any given channel condition.

3) Tracking Channel Changes: Our solution inherently tracks changes on the line in real time as a consequence of using the LMS adaptive filter. However, on encountering a channel change, the filter requires an additional transient

time to reach its saturation value, when it can provide the maximum possible ECG. This transient time is dependent on the step-size of the LMS adaptation algorithm, and also on the channel and noise conditions. For typical PLC network conditions, the transient time is shown to be around 1.5% of the time between two different channel conditions on a busy power line network [15]. Since we use the same LMS adaptation procedure, we expect to encounter similar values of transient time. Apart from such long-term channel changes, power lines are also subject to short-terms changes, which are linear periodically time varying (LPTV) in nature [47]. To adapt to such changes, the LMS filters use a customized LPTV-LMS algorithm that we previously developed in [15]. Since our AIC solution estimates the echo channel digitally, it is capable of quickly adapting and reconfiguring the filter weights to changing network conditions.

4) Application Scenarios: Throughout our work, we provide analyses and results for a point-to-point communication link. However, it is straightforward to adopt our solution to other scenarios, like full-duplex relaying, or full-duplex spectrum sensing [48], [49]. Since our solution requires no wait times or dedicated pilot/training signals, it provides a seamless full-duplex relaying operation without any initialization period. Further, while using our solution for simultaneous transmission and spectrum sensing, the maximal ECG can be achieved under all conditions, since the signal being monitored is only the noise on the line and not a PLC signal [25].

5) Processor and DAC Complexity: In our simulations and analyses, we consider the transceiver processor and the DACs used in the transmission and echo reconstruction chains to have sufficient precision to replicate an analog channel digitally. From Fig. 8, we observe that this precision needs to be at least 16 bits to obtain a signal-to-noise-and-distortion ratio of over 80 dB. If a lower resolution DAC is used in the transmitter chain, it introduces additional distortion and quantization noise. However, this can be countered by tapping the transmitted signal after the DAC quantizer module for use at the LMS filter (see Figs. 1 and 3), so that the input signal entering the filter already consists of the DAC distortion and quantization noise effects [50]. Further, to avoid similar such effects, the echo reconstruction chain demands a high-resolution DAC of 16 bits or more. This solution also requires an additional DFT block to convert the tapped time domain signal into a frequency domain input to the LMS filter.

B. Implementation Costs

SI cancellation in the analog domain requires the use of an analog adder. This can be implemented using an active operational amplifier (op-amp) based differential amplifier circuit to ensure no additional signal power loss. Due to the large amplitude of PLC signals and a tight restriction on the non-linear SI cancellation, a wide voltage range, low distortion op-amp such as LMH6702 [37] is appropriate. A similar op-amp is also required to build the active hybrid circuit. With a maximum PLC signal voltage of ± 6 V [39], and an op-amp supply current of 12.5 mA [37], the adder and hybrid together consume an additional power of 225 mW. For an $N_{\mathrm{T}} \times N_{\mathrm{R}}$ MIMO IBFD system, this value is scaled by a factor of N_{T}, and an additional power of $(N_{\mathrm{R}} - N_{\mathrm{T}}) \cdot 75$ mW is required for the analog adders in the stand-alone receiver chains.

Apart from these AFE overheads, the companion PHY/MAC transceiver chip set will also require N_{R} additional DACs. Commercially available DACs of 18-bit resolution consume about 4 mW each [51]. Unlike the DIC solution, the additional power consumption by the analog adders and the DACs are specific to our AIC solutions. However, the computation overhead introduced by the LMS adaptation filters applies equally for both the DIC and AIC solutions. For the system parameters specified in the HomePlug AV standard [40], the frequency-domain LMS adaption procedure requires about $7,369$ million operations per second (MOPS) [15, Table I]. The additional power consumption introduced by these operations depends on the type of processor implementation. It has been shown that newer processor architectures are able to provide an energy efficiency of 970 MOPS per mW [52, Ch. 5]. Therefore, the additional processor power consumption can be computed to be $\left(N_{\mathrm{T}} \cdot N_{\mathrm{R}} \cdot \frac{7,369}{970}\right)$ mW. We present the overall comparative power consumption overheads associated with the DIC and our proposed AIC solutions in Table II.

In total, the overall increase in power consumption for a 2×4 MIMO IBFD BB-PLC system is less than 0.7 W. Considering that the device is always connected to the power line, and that the typical power consumption of a HD MIMO BB-PLC device is about 8 W [53], this additional power requirement adds a relatively small overhead.

VIII. Conclusions

In this paper, we have proposed an IBFD solution for BB-PLC devices using an op-amp based hybrid for suppression and an adaptive analog cancellation procedure. By canceling the echo in the analog domain, we successfully countered the critical constraint imposed by the distortion and quantization noise introduced in the ADC. Further, we extended our solution to a MIMO BB-PLC system and analytically characterized the echo channel transfer function by illustrating the PLC signal coupling mechanism for an IBFD-enabled MIMO BB-PLC transceiver. With our proposed solution, we showed the benign effects of the residual non-linear SI components on the signal-of-interest. Using realistic power line channel and noise settings, we demonstrated through simulation results that our solution is capable of successfully doubling median data rates under typical in-home power line network conditions in a SISO configuration, and achieve at least a 1.8 times median data rate gain in the MIMO mode.

Appendix A
An Approximate Expression for γ_{ADC}

In this appendix, we formulate an approximate expression of γ_{ADC} for an ADC operation that incorporates signal clipping of high PAPR OFDM signals, in order to minimize the overall distortion and quantization noise power. We begin with the

TABLE II
ADDITIONAL POWER CONSUMPTION OVERHEAD FOR DIC [15] AND OUR PROPOSED AIC SOLUTIONS

	SISO				2×4 MIMO			
Component	DIC		AIC		DIC		AIC	
	Quantity	Power (mW)	Quantity	Power (mW)	Quantity	Power (mW)	Quantity	Power (mW)
Hybrid	1	150	1	150	2	300	2	300
Additional DAC	0	0	1	4	0	0	4	16
Analog adder	0	0	1	75	0	0	4	300
LMS filter	1	7.6	1	7.6	8	60.8	8	60.8
Total		**157.6**		**236.6**		**360.8**		**676.8**

exact relation of (8), and express it in logarithmic scale as

$$\gamma_{\mathrm{ADC,dB}} = -10 \cdot \log_{10}\left(\frac{1/3}{2^{2m}}\left(\frac{V_{\mathrm{clip}}}{\sigma_{\mathrm{inp}}}\right)^2 + \sqrt{\frac{8}{\pi}}\left(\frac{\sigma_{\mathrm{inp}}}{V_{\mathrm{clip}}}\right)^3 \exp\left(\frac{-{V_{\mathrm{clip}}}^2}{2\sigma_{\mathrm{inp}}^2}\right)\right). \quad (21)$$

It is evident from (21) that $\gamma_{\mathrm{ADC,dB}}$ is dependent on the clipping ratio, $\frac{V_{\mathrm{clip}}}{\sigma_{\mathrm{inp}}}$. It has been shown that the optimal clipping ratio, $\left(\frac{V_{\mathrm{clip}}}{\sigma_{\mathrm{inp}}}\right)_{\mathrm{opt}}$, nearly varies quadratically with m, and that its least squares fit can be expressed as $\left(\frac{V_{\mathrm{clip}}}{\sigma_{\mathrm{inp}}}\right)_{\mathrm{opt}} = \alpha m^2 + \beta m + \delta$, where α, β, and δ are the quadratic polynomial coefficients [54]. By tuning our Gain Control to force the PGA to consistently provide this optimal clipping ratio of the received signal to the ADC, we can rewrite (21) as

$$\gamma_{\mathrm{ADC,dB}} = -10 \cdot \log_{10}\left(\frac{\left(\alpha m^2 + \beta m + \delta\right)^2}{3 \cdot 2^{2m}} + \frac{\sqrt{\frac{8}{\pi}}}{\left(\alpha m^2 + \beta m + \delta\right)^3} \exp\left(\frac{-\left(\alpha m^2 + \beta m + \delta\right)^2}{2}\right)\right). \quad (22)$$

It is clear from (22) that $\gamma_{\mathrm{ADC,dB}}$ is not strictly linearly with m. However, a plot of $\gamma_{\mathrm{ADC,dB}}$ versus m in Fig. 8 shows that $\gamma_{\mathrm{ADC,dB}}$ is nearly linear in m. We can therefore find an approximate linear expression for $\gamma_{\mathrm{ADC,dB}}$ using a first-order Taylor series expansion of (22).

Since we use a 12-bit ADC, we evaluate the first order Taylor series expansion of $\gamma_{\mathrm{ADC,dB}}$ at $m = 12$. By using $\{\alpha, \beta, \delta\} = \{-0.0053, 0.3763, 1.2627\}$ [54], we find the linear approximation for $\gamma_{\mathrm{ADC,dB}}$ to be

$$\hat{\gamma}_{\mathrm{ADC,dB}} = 5.5m - 3.6. \quad (23)$$

We observe from Fig. 8 that this approximation provides a close fit to (22).

APPENDIX B
ADC BITS LOST IN IBFD

This derivation of the number of ADC bits lost with an IBFD operation follows a similar derivation in [55]. However, we use the $\hat{\gamma}_{\mathrm{ADC,dB}}$ expression derived in Appendix A and the system model described in Section III.

The additional ADC bits lost due to IBFD can be expressed as the difference between the loss of bits for quantizing the

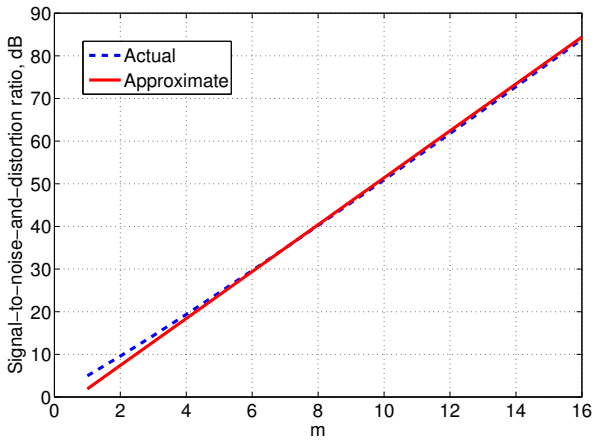

Fig. 8. Variation of $\gamma_{\mathrm{ADC,dB}}$ from (22) and $\hat{\gamma}_{\mathrm{ADC,dB}}$ of (23) with m.

SOI in HD and IBFD modes. Therefore, we use (10) to write

$$b_{\mathrm{lost}} = \frac{10}{5.5}\left(\log_{10}\left(\frac{\sigma_{\mathrm{inp,FD}}^2}{P_{\mathrm{TX}}G_{\mathrm{PLC}}}\right) - \log_{10}\left(\frac{\sigma_{\mathrm{inp,HD}}^2}{P_{\mathrm{TX}}G_{\mathrm{PLC}}}\right)\right) = \lambda \cdot \log_{10}\left(\frac{\sigma_{\mathrm{inp,FD}}^2}{\sigma_{\mathrm{inp,HD}}^2}\right), \quad (24)$$

where $\lambda = {}^{20}/_{11}$.

SISO: For a point-to-point SISO link, $\sigma_{\mathrm{inp,FD}}^2 = P_{\mathrm{TX}}(G_{\mathrm{total}} + G_{\mathrm{PLC}}) + P_{\mathrm{N}}$, and $\sigma_{\mathrm{inp,HD}}^2 = P_{\mathrm{TX}}G_{\mathrm{PLC}} + P_{\mathrm{N}}$. We can thus re-write (24) as

$$b_{\mathrm{lost}} = \lambda \cdot \log_{10}\left(1 + \frac{P_{\mathrm{TX}}G_{\mathrm{total}}}{P_{\mathrm{TX}}G_{\mathrm{PLC}} + P_{\mathrm{N}}}\right). \quad (25)$$

MIMO: For a MIMO scenario, $\sigma_{\mathrm{inp,FD},i}^2 = P_{\mathrm{TX}}\left(\sum_{j=1}^{N_{\mathrm{T}}^{\mathrm{near}}} G_{\mathrm{total},ij} + \sum_{j=1}^{N_{\mathrm{T}}^{\mathrm{far}}} G_{\mathrm{PLC},ij}\right) + P_{\mathrm{N},i}$ and $\sigma_{\mathrm{inp,HD},i}^2 = P_{\mathrm{TX}}\sum_{j=1}^{N_{\mathrm{T}}^{\mathrm{far}}} G_{\mathrm{PLC},ij} + P_{\mathrm{N},i}$, at the ith receiver. Hence, (24) for MIMO can be re-written for the ith receiver as

$$b_{\mathrm{lost},i} = \lambda \cdot \log_{10}\left(1 + \frac{P_{\mathrm{TX}}\sum_{j=1}^{N_{\mathrm{T}}^{\mathrm{near}}} G_{\mathrm{total},ij}}{P_{\mathrm{TX}}\sum_{j=1}^{N_{\mathrm{T}}^{\mathrm{far}}} G_{\mathrm{PLC},ij} + P_{\mathrm{N},i}}\right). \quad (26)$$

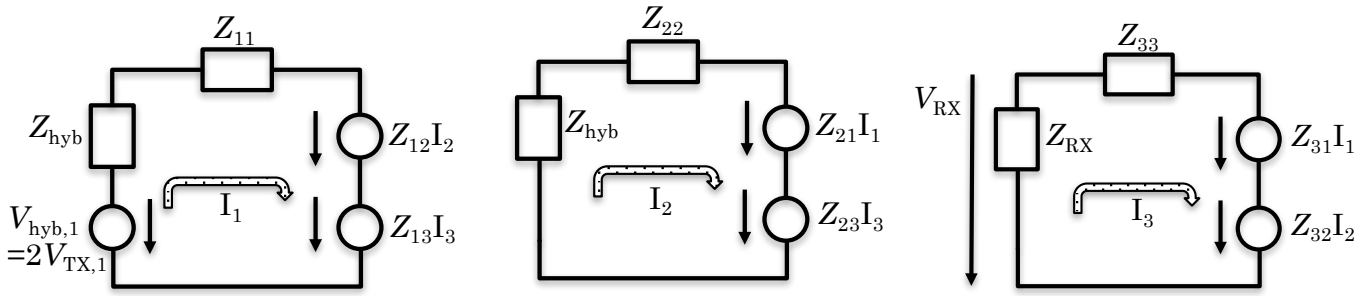

Fig. 9. Equivalent circuits of the power line-hybrid interface (shown in red in Fig. 2) using the Z-parameters described by the input impedance matrix of the power line.

APPENDIX C
INTERFERENCE CHANNEL TRANSFER FUNCTIONS AT THE STAND-ALONE RECEIVER

In this appendix, we consider a 2×3 MIMO transceiver and derive the channel transfer functions of the two CI channels at the stand-alone receiver (i.e., operating without an associated transmitter). Throughout this derivation, we consider a frequency selective interference channel created as a result of a frequency selective network impedance. However, we drop the frequency index for brevity.

We first derive the interference channel transfer function from the first transceiver to the stand-alone receiver. To aid our derivation, we decompose the line-hybrid interface (shown in red in Fig. 2) into three equivalent circuits shown in Fig. 9, by viewing the interface as a three port network whose Z-parameters are described by the power line input impedance matrix,

$$\mathbf{Z}_{\text{PLC}} = \begin{bmatrix} Z_{11} & Z_{12} & Z_{13} \\ Z_{21} & Z_{22} & Z_{23} \\ Z_{31} & Z_{32} & Z_{33} \end{bmatrix}. \tag{27}$$

Fig. 9(a) shows the equivalent circuit at the first transceiver. We replace the hybrid with its Thevenin equivalent source voltage and impedance. Since the hybrid is designed to completely transfer voltage from one port to a matched load at the adjacent port in one direction [15], [56], the Thevenin equivalent voltage of the hybrid, $V_{\text{hyb},1} = 2V_{\text{TX},1}$, where $V_{\text{TX},1}$ is the signal voltage at the hybrid port connected to the transmitter. The Thevenin equivalent impedance is the hybrid impedance shown to the power line, $Z_{\text{hyb}} = 100\ \Omega$, which is set to match the typical power line impedance. At the second transceiver, shown in Fig. 9(b), we short the voltage source in accordance with the superposition theorem, and replace the hybrid with its Thevenin equivalent impedance of Z_{hyb}. Finally, we represent the stand-alone receiver with its impedance of Z_{RX} in Fig. 9(c).

Applying Kirchoff's voltage law in these three circuits provides us

$$I_1(Z_{\text{hyb}} + Z_{11}) + I_2 Z_{12} + I_3 Z_{13} = 2V_{\text{TX},1}, \tag{28}$$
$$-I_1 Z_{21} - I_2(Z_{\text{hyb}} + Z_{22}) - I_3 Z_{23} = 0, \tag{29}$$
$$-I_1 Z_{31} - I_2 Z_{32} - I_3(Z_{\text{RX}} + Z_{33}) = 0, \tag{30}$$

where I_1, I_2, and I_3 are the currents flowing in the circuits of Fig. 9(a), Fig. 9(b), and Fig. 9(c), respectively. Further, we have the voltage drop at the stand-alone receiver,

$$V_{\text{RX}} = -I_3 Z_{\text{RX}}. \tag{31}$$

By solving the three equations (28), (29), and (30) for three unknowns I_1, I_2, and I_3, and by using (31), we obtain the CI transfer function from the first transmitter to the stand-alone receiver as

$$\frac{V_{\text{RX}}}{V_{\text{TX},1}} = \frac{-2Z_{\text{RX}}}{(\delta_{31} + \delta_{21}\delta_{32})(Z_{\text{hyb}} + Z_{11}) + Z_{12}\delta_{32} + Z_{13}}, \tag{32}$$

where

$$\delta_{31} = -\frac{Z_{\text{RX}} + Z_{33}}{Z_{31}} \tag{33}$$
$$\delta_{21} = -\frac{Z_{32}}{Z_{31}} \tag{34}$$
$$\delta_{32} = -\frac{Z_{23} + Z_{21}\delta_{31}}{Z_{\text{hyb}} + Z_{22} + \delta_{21}Z_{21}}. \tag{35}$$

Next, we represent this transfer function in terms of the reflection co-efficient at the line-hybrid interface. The transceiver impedance matrix, $\mathbf{Z}_{\text{TR}}$, as seen from the line can be written as

$$\mathbf{Z}_{\text{TR}} = \begin{bmatrix} Z_{\text{hyb}} & 0 & 0 \\ 0 & Z_{\text{hyb}} & 0 \\ 0 & 0 & Z_{\text{RX}} \end{bmatrix}. \tag{36}$$

We then have the reflection co-efficient matrix at the line-hybrid interface as

$$\begin{aligned} \mathbf{\Gamma}_{\text{PLC}} &= \begin{bmatrix} \Gamma_{11} & \Gamma_{12} & \Gamma_{13} \\ \Gamma_{21} & \Gamma_{22} & \Gamma_{23} \\ \Gamma_{31} & \Gamma_{32} & \Gamma_{33} \end{bmatrix} \\ &= (\mathbf{Z}_{\text{PLC}} - \mathbf{Z}_{\text{TR}})(\mathbf{Z}_{\text{PLC}} + \mathbf{Z}_{\text{TR}})^{-1}. \end{aligned} \tag{37}$$

Simplifying (37) using (27) and (36) reveals that $\frac{V_{\text{RX}}}{V_{\text{TX},1}} = \Gamma_{31}$. Similarly, we also obtain the interference channel transfer function from the second transmitter to the stand-alone receiver as $\frac{V_{\text{RX}}}{V_{\text{TX},2}} = \Gamma_{32}$.

REFERENCES

[1] G. Prasad, L. Lampe, and S. Shekhar, "Analog interference cancellation for full-duplex broadband power line communications," in *IEEE Intl. Symp. on Power Line Commun. Appl. (ISPLC)*, Apr. 2017.

[2] ——, "Enhancing transmission efficiency of broadband plc systems with in-band full duplexing," in *IEEE Intl. Symp. Power Line Commun. and Its Appl. (ISPLC)*, 2016, pp. 46–51.

[3] J. I. Choi, M. Jain, K. Srinivasan, P. Levis, and S. Katti, "Achieving single channel, full duplex wireless communication," in *ACM MOBICOM*, 2010, pp. 1–12.

[4] A. Sabharwal, P. Schniter, D. Guo, D. W. Bliss, S. Rangarajan, and R. Wichman, "In-band full-duplex wireless: Challenges and opportunities," *IEEE J. Sel. Areas Commun.*, vol. 32, no. 9, pp. 1637–1652, 2014.

[5] S. Weinstein, "Echo cancellation in the telephone network," *IEEE Commun. Mag.*, vol. 15, no. 1, pp. 8–15, Jan. 1977.

[6] A. G. Stove, "Linear FMCW radar techniques," in *IEE Proceedings F-Radar and Signal Processing*, vol. 139, no. 5. IET, 1992, pp. 343–350.

[7] W. Y. Chen, J. L. Dixon, and D. L. Waring, "High bit rate digital subscriber line echo cancellation," *IEEE J. Sel. Areas Commun.*, vol. 9, no. 6, pp. 848–860, 1991.

[8] T.-C. Lee and B. Razavi, "A 125-MHz mixed-signal echo canceller for gigabit ethernet on copper wire," *IEEE J. Solid-State Circuits*, vol. 36, no. 3, pp. 366–373, 2001.

[9] R. Mahadevan, "A front-end circuit for full-duplex transmission over coaxial cable." Ph.D. dissertation, University of Toronto, 2001.

[10] M. Duarte, C. Dick, and A. Sabharwal, "Experiment-driven characterization of full-duplex wireless systems," *IEEE Trans. Wireless Commun.*, vol. 11, no. 12, pp. 4296–4307, 2012.

[11] E. Tsakalaki, E. Foroozanfard, E. De Carvalho, and G. F. Pedersen, "A 2-order MIMO full-duplex antenna system," in *IEEE European Conf. Antennas and Propagation (EuCAP)*, 2014.

[12] D. Bharadia, E. McMilin, and S. Katti, "Full duplex Radios," in *ACM SIGCOMM*, 2013, pp. 375–386.

[13] Y.-S. Choi and H. Shirani-Mehr, "Simultaneous transmission and reception: Algorithm, design and system level performance," *IEEE Trans. Wireless Commun.*, vol. 12, no. 12, pp. 5992–6010, 2013.

[14] N. Ehtiati and B. Champagne, "A general framework for mixed-domain echo cancellation in discrete multitone systems," *IEEE Trans. Commun.*, vol. 61, no. 2, pp. 769–780, 2013.

[15] G. Prasad, L. Lampe, and S. Shekhar, "In-band full duplex broadband power line communications," *IEEE Trans. Commun.*, vol. 64, no. 9, pp. 3915–3931, Sept 2016.

[16] C. Tripodi, G. Ferrari, R. Pighi, and R. Raheli, "A novel weight reset strategy for the LMS algorithm subject to abrupt channel variations," in *IEEE Intl. Symp. Power Line Commun. and Its Appl. (ISPLC)*, 2015, pp. 131–136.

[17] "IEC 62488-1:2012: Power line communication systems for power utility applications," *International Electrotechnical Commission*. [Online]. Available: https://webstore.iec.ch/publication/7095

[18] T. Esmailian, F. Kschischang, and P. Gulak, "In-building power lines as high-speed communication channels: channel characterization and a test channel ensemble," *Int. J. Commun. Syst.*, vol. 16, no. 5, pp. 381–400, 2003.

[19] G. Prasad, H. Ma, M. J. Rahman, F. Aalamifar, and L. Lampe. A cumulative power line noise generator. [Online]. Available: http://www.ece.ubc.ca/~gauthamp/PLCnoise

[20] S. Galli, H. Latchman, V. Oksman, G. Prasad, and L. Yonge, "Multimedia PLC systems," in *Power Line Communications: Principles, Standards and Applications from Multimedia to Smart Grid*, L. Lampe, A. Tonello, and T. Swart, Eds. John Wiley and Sons Ltd, 2016, ch. 8, pp. 475 – 511.

[21] A. Sahai, G. Patel, and A. Sabharwal, "Pushing the limits of full-duplex: Design and real-time implementation," *arXiv preprint arXiv:1107.0607*, 2011.

[22] S. K. Gupta, J. Tellado, S. Begur, F. Yang, M. A. Inerfield *et al.*, "10GBASE-T for 10Gb/s full duplex ethernet LAN transmission over structured copper cabling," in *IEEE Radio Frequency Integrated Circuits Symposium (RFIC)*, 2008, pp. 203–206.

[23] S. Gupta, J. Tellado, S. Begur, F. Yang, V. Balan *et al.*, "A 10Gb/s IEEE 802.3 an-compliant ethernet transceiver for 100m UTP cable in 0.13 μm CMOS," in *IEEE International Solid-State Circuits Conference (ISSCC)*, 2008.

[24] M. Duarte, A. Sabharwal, V. Aggarwal, R. Jana, K. Ramakrishnan, C. W. Rice, and N. Shankaranarayanan, "Design and characterization of a full-duplex multiantenna system for WiFi networks," *IEEE Trans. Veh. Tech.*, vol. 63, no. 3, pp. 1160–1177, 2014.

[25] G. Prasad and L. Lampe, "Full-duplex spectrum sensing for broadband power line communications," in *IEEE Intl. Symp. Power Line Commun. and its Appl. (ISPLC)*, Apr. 2017.

[26] S. Haykin, *Adaptive filter theory*. 2nd. ed., Prentice-Hall, Englewood Cliffs, NJ, 1991.

[27] D. Dardari, "Joint clip and quantization effects characterization in OFDM receivers," *IEEE Trans. Circuits Syst. I: Regular Papers*, vol. 53, no. 8, pp. 1741–1748, 2006.

[28] D. J. Mestdagh, P. M. Spruyt, and B. Biran, "Effect of amplitude clipping in DMT-ADSL transceivers," *IET Electronics Letters*, vol. 29, no. 15, pp. 1354–1355, 1993.

[29] L. T. Berger, A. Schwager, P. Pagani, and D. Schneider, *MIMO Power Line Communications: Narrow and Broadband Standards, EMC, and Advanced Processing*. CRC Press, 2014.

[30] R. C. Mullin and P. Simmons, *Electrical Wiring Commercial*. Cengage Learning, 2012.

[31] L. Yonge, J. Abad, K. Afkhamie, L. Guerrieri, S. Katar, H. Lioe, P. Pagani, R. Riva, D. M. Schneider, and A. Schwager, "An overview of the homeplug AV2 technology," *J. of Elect. and Comput. Eng.*, 2013.

[32] International Telecommunications Union (ITU), "ITU-T Recommendation G.9963, Unified high-speed wire-line based home networking transceivers - Multiple Input/Multiple Output (MIMO)," Sep. 2011, (ex G.hn-MIMO).

[33] D. Righini and A. Tonello, "Broadband MIMO couplers characterization and comparison," in *Tenth Annu. Workshop on Power Line Commun. (WSPLC)*, Oct. 2016.

[34] L. Ding, "Digital predistortion of power amplifiers for wireless applications," Ph.D. dissertation, Georgia Institute of Technology, 2004.

[35] F. H. Gregorio, "Analysis and compensation of nonlinear power amplifier effects in multi-antenna OFDM systems," Ph.D. dissertation, Helsinki University of Technology, 2007.

[36] Intersil ISL1571 datasheet. [Online]. Available: http://www.intersil.com/content/dam/Intersil/documents/isl1/isl1571.pdf

[37] LMH6702 1.7-GHz ultra-low distortion wideband op amp. [Online]. Available: http://www.ti.com/lit/ds/symlink/lmh6702.pdf

[38] H. A. Latchman, S. Katar, L. Yonge, and S. Gavette, *Homeplug AV and IEEE 1901: A Handbook for PLC Designers and Users*. Wiley-IEEE Press, 2013.

[39] "IEEE standard for broadband over power line networks: Medium access control and physical layer specifications," *IEEE Std 1901-2010*, pp. 1–1586, Dec 2010.

[40] "Homeplug AV specification, version 1.1," *HomePlug Powerline Alliance*, pp. 1 – 673, May 2007.

[41] G. Marrocco, D. Statovci, and S. Trautmann, "A PLC broadband channel simulator for indoor communications," in *IEEE Intl. Symp. Power Line Commun. and Its Appl. (ISPLC)*, 2013, pp. 321–326.

[42] A. M. Tonello and F. Versolatto, "Bottom-up statistical PLC channel modeling—Part I: Random topology model and efficient transfer function computation," *IEEE Trans. Power Del.*, vol. 26, no. 2, pp. 891–898, 2011.

[43] F. Gruber and L. Lampe, "On PLC channel emulation via transmission line theory," in *IEEE Intl. Symp. Power Line Commun. and Its Appl. (ISPLC)*, Austin, TX, USA, 2015. [Online]. Available: http://www.ece.ubc.ca/~lampe/MIMOPLC

[44] C. R. Paul, *Analysis of multiconductor transmission lines*. John Wiley & Sons, 2008.

[45] F. Versolatto and A. M. Tonello, "An MTL theory approach for the simulation of MIMO power-line communication channels," *IEEE Trans. on Power Del.*, vol. 26, no. 3, pp. 1710–1717, 2011.

[46] S. T. Chung and A. J. Goldsmith, "Degrees of freedom in adaptive modulation: a unified view," *IEEE Trans. Commun.*, vol. 49, no. 9, pp. 1561–1571, 2001.

[47] F. J. Cañete, J. A. Cortés, L. Díez, and J. T. Entrambasaguas, "Analysis of the cyclic short-term variation of indoor power line channels," *IEEE J. Sel. Areas Commun.*, vol. 24, no. 7, pp. 1327–1338, 2006.

[48] G. Liu, F. Yu, H. Ji, V. Leung, and X. Li, "In-band full-duplex relaying: A survey, research issues and challenges," *IEEE Commun. Surveys Tuts.*, vol. 17, no. 2, pp. 500–524, Secondquarter 2015.

[49] W. Cheng, X. Zhang, and H. Zhang, "Imperfect full duplex spectrum sensing in cognitive radio networks," in *ACM CoRoNet*, 2011, pp. 1–6.

[50] P. J. Hurst and A. Norrell, "DAC quantization-noise cancellation in an echo-canceling transceiver," *IEEE Trans. Circuits and Syst. II: Express Briefs*, vol. 55, no. 2, pp. 111–115, 2008.

[51] DAC9881 18-bit, single-channel, low-noise, voltage-output digital-to-analog converter. [Online]. Available: http://www.ti.com/lit/ds/symlink/dac9881.pdf

[52] R. Fasthuber, F. Catthoor, P. Raghavan, and F. Naessens, *Energy-efficient communication processors*. Springer, 2013.
[53] Devolo dLAN 1200+ WiFi ac. [Online]. Available: http://www.devolo.com/products/dLAN-WLAN/dLAN-1200+-WiFi-ac/data/Data-sheet-dLAN-1200+-WiFi-ac-com.pdf
[54] H. Ehm, S. Winter, and R. Weigel, "Analytic quantization modeling of OFDM signals using normal Gaussian distribution," in *Asia-Pacific Microwave Conference*, Dec 2006, pp. 847–850.
[55] D. Korpi, T. Riihonen, V. Syrjälä, L. Anttila, M. Valkama, and R. Wichman, "Full-duplex transceiver system calculations: Analysis of ADC and linearity challenges," *IEEE Trans. Wireless Commun.*, vol. 13, no. 7, pp. 3821–3836, 2014.
[56] C. Wenzel, "Low frequency circulator/isolator uses no ferrite or magnet," *RF Design (1991)*, pp. 39–43.